# Ambiguity Free Doppler Velocity Decomposed Imaging Method for 79 GHz Band Millimeter Wave Radar

Yoshiki Sekigawa and Shouhei Kidera, *Senior Member, IEEE*

Abstract—**This paper proposes an accurate Doppler velocity–associated radar imaging method for millimeter wave short-range radar. Doppler velocity–based data decomposition is promising in terms of enhancing the spatial resolution of radar images, especially for multiple objects with different motion velocities, *e.g.*, human walking models. However, the traditional short-time Fourier transform (STFT) or other time–frequency analysis methods inherently suffer from inaccuracy due to a limited unambiguous velocity range or the trade-off between temporal and frequency resolutions. To address this problem, the proposed method incorporates time-of-flight (TOF) based Doppler velocity estimation, *i.e.*, the weighted kernel density (WKD) method, which overcomes the limitations of unambiguous velocity range and the trade-off between temporal and frequency resolutions in the Doppler velocity decomposed and associated radar imaging. Experimental results obtained using 79-GHz band MMW radar equipment demonstrate the effectiveness of the proposed method for two use cases, *i.e.*, multiple rotating spheres and a human walking model.**

Index Terms—**79 GHz millimeter wave (MMW) band radar, multiple-input-multiple-output (MIMO) radar, Doppler associated radar imaging, Weighted kernel density estimator (WKD), Micro-Doppler velocity estimation, Human body imaging.**
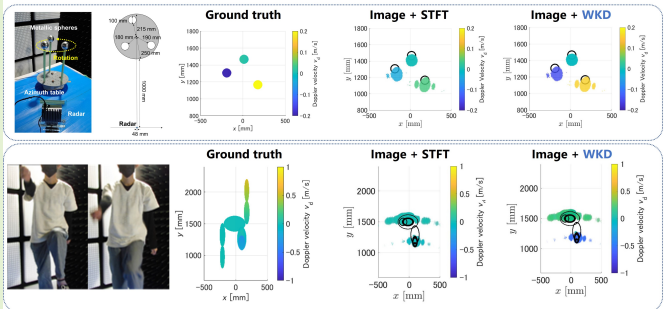
I. INTRODUCTION

With the increasing prevalence of self-driving and advanced driver assistance systems (ADAS) , developers have introduced various environmental sensors. For example, high-frequency millimeter wave (MMW) radar is a cutting-edge sensing technique that boasts numerous advantages, *e.g.*, high spatial resolution and compact modules [1], [2]. MMW radar also shows promise as an environmentally robust sensor that is applicable in situations where optical visibility is severely limited, *e.g.*, dense smog or adverse weather conditions. Despite these advantages, MMW radar imaging faces challenges in terms of spatial resolution limitations imposed by the aperture size. This limitation is problematic in vehicle-mounted radar systems because the aperture size cannot be expanded considerably because a target, *e.g.*, a pedestrian or car, should be positioned in front of the radar. In far-range sensing cases exceeding 10 m, the aperture angle

becomes critically small, which makes it difficult to achieve the required spatial resolution for effective object recognition.

Several radar imaging schemes assuming the MMW multi-input-multi-ouput (MIMO) observation model employ a co-herent integration (CI) approaches like the Kirchhoff migration [3], [4], the range migration algorithm (RMA) [5]–[8], and sparse regularization schemes [9]–[12]. However, these methods face challenges due to limited spatial resolution, which would be more critical in situations with small aperture angles, as assumed in the frontline sensing scenario in automotive radar. To address with the above-mentioned issue, a number of studies have been developed focusing on the micro-Doppler velocity analysis [13]–[16] for the human body or gait level recognition via the machine learning approaches [17]–[19]. However, there are a limited number of studies focusing on Doppler-associated radar imaging schemes like [13], while a greater number of studies have focused on enhancing the equivalent range resolutions through Doppler spectra decomposition [20]. A recent study [21], [22] introduced the Doppler velocity decomposed CI imaging approach focusing on the advantages of the higher MMW band, *e.g.*, the 79 GHz band, which can offer much higher Doppler velocity resolution, even with a short coherent

processing interval (CPI). This further enhances the equivalent spatial resolution when dealing multiple objects with different motion velocities, *e.g.*, the human walking motion.

Thus, in this paper, we introduce a Doppler velocity decomposed radar imaging scheme. Note that the previous method [21], [22] employs short-time-Fourier transform (STFT)-based time–frequency analysis to estimate the Doppler spectra, which are associated with radar images. However, these Doppler velocities are inherently limited within an unambiguous Doppler velocity range, which is strictly determined by the pulse repetition interval (PRI) under the Nyquist condition. Thus, if a sufficiently short PRI cannot be acquired in the actual radar module, it would be difficult to estimate the Doppler velocity for moving objects with a velocity greater than the unambiguous Doppler velocity. This scenario could occur in a human walking model. For example, assuming a 79-GHz MMW with a PRI of 10 ms, the unambiguous velocity should be ± 0.1 m/s, which is considerably less than the actual motion of each body part (arm or leg) with over 1.0 m/s velocity.

To address the above-mentioned issue, this study introduces a novel scheme by combining a weighted kernel density (WKD) Doppler velocity estimator [23] and the Doppler decomposed radar imaging [22] to retain accurate Doppler velocity associated imaging, especially for a walking human model. The WKD method [23] converts the discrete time-of-flight (TOF) values associated with slow time as τ, the so-called range-τ points, to the Doppler velocity points using a kernel density-based probability density function estimator, and it offers several distinct advantages. For example, there is no limitation on the Doppler velocity and temporal resolution or the unambiguous velocity range because the Doppler velocity is defined simply by the inclination of neighboring range-τ points. In addition, the challenging procedure to connect multiple range-τ points can be avoided by evaluating all range-τ points with a weighting function, which allows for batch processing. We associate the point cloud-based WKD outputs with the decomposed distributed radar image in the proposed method by focusing on the distinct advantages of the WKD method. This method enhances the accuracy of the Doppler velocity estimation because it is free from the limitation of unambiguous range. Notably, previous studies have used the WKD method [24], where the range points migration (RPM) [25] radar imaging scheme was incorporated; however, the RPM image cannot retain sufficient angular resolution at the higher frequencies, such as in the 79 GHz band, because it is based on an incoherent integration process. Thus, it is necessary to integrate a CI-based radar image with the WKD based Doppler velocity estimator to achieve both high spatial resolution imaging and ambiguity-free Doppler velocity estimation.

Thus, the primary contributions of this study are summarized as follows.

1) The Doppler decomposed and associated radar imaging scheme contributes to higher resolution and multi-functional imaging, which is beneficial for human
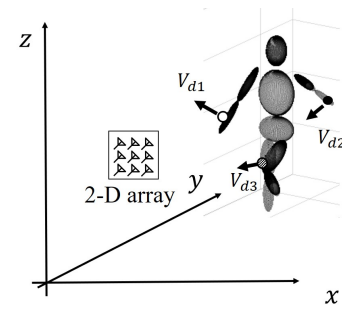

Fig. 1: Observation model.

walking models with micro-Doppler components in each part.

2) The WKD based Doppler velocity estimation overcomes the limitation of the unambiguous velocity range, which is strictly determined by the PRI and the wavelength in the traditional STFT based Doppler analysis scheme used in [22].

3) Experimental tests using three rotating spheres and a real human walking model demonstrate that accurate and high spatial resolution radar imaging associated with Doppler velocity can be realized using a commercial 79-GHz frequency modulated continuous wave (FMCW) MIMO radar module.

II. METHOD

A. Observation Model

The observation model employed in the proposed method is shown in Fig. 1. Here, we assume MIMO radar imaging, and multiple transmitters and receivers are located in a planar array, placed on the $y = 0$. Then, the locations of the transmitter and receiver are defined as $\boldsymbol{r}_{\mathrm{T}} = (x_{\mathrm{T}}, 0, z_{\mathrm{T}})$ and $\boldsymbol{r}^{\mathrm{R}} = (x_{\mathrm{R}}, 0, z)$, respectively. The modulated pulse is transmitted repeatedly with a constant PRI, and a slow time τ is indexed by the PRI. In addition, $s(\boldsymbol{r}_{\mathrm{T}}, \boldsymbol{r}_{\mathrm{R}}, R, \tau)$ is defined as the complex scattered signal at each transmitter and receiver combination, where $R = ct/2$ holds with the fast time t and the radio-wave speed c. If a complex electric field as $s(\boldsymbol{r}_{\mathrm{T}}, \boldsymbol{r}_{\mathrm{R}}, R, \tau)$ can be observed, either pulse-Doppler radar or FMCW radar systems are applicable to the proposed method. Furthermore, the $s(\boldsymbol{r}_{\mathrm{T}}, \boldsymbol{r}_{\mathrm{R}}, R, \tau)$ is truncated along slow time τ for post-Doppler analysis with a CPI, and is defined as $s(\boldsymbol{r}_{\mathrm{T}}, \boldsymbol{r}_{\mathrm{R}}, R, \tau; \tau_m)$, where τ_m denotes the center of each CPI.

B. Conventional Doppler Velocity Decomposed Radar Imaging

In the case of vehicle-mounted radar, the available aperture size of the array is frequently limited to maintain a sufficient azimuth resolution, which is a challenging issue in several cases, *e.g.*, when decomposing each part of the human body in short-range scenarios. To address this difficulty, our previous study [21], [22] introduced the Doppler decomposition based radar imaging, to retain interference-robust and multi-functional radar imaging. Here, we briefly introduce the

methodology as follows: In the first step, the measured data as $\tilde{s}(\boldsymbol{r}_\mathrm{T}, \boldsymbol{r}_\mathrm{R}, R, \tau; \tau_m)$ are converted to the $R - v_\mathrm{d}$ space by the 1D FT as follows:

$$S(\boldsymbol{r}_\mathrm{T}, \boldsymbol{r}_\mathrm{R}, R, v_\mathrm{d}; \tau_m) = \int_T \tilde{s}(\boldsymbol{r}_\mathrm{T}, \boldsymbol{r}_\mathrm{R}, R, \tau; \tau_m)e^{-j\omega\tau}\mathrm{d}\tau, \tag{1}$$

Here, T denotes the CPI, and $v_\mathrm{d} = \omega\lambda/4\pi$ is defined, where λ denotes the wavelength of the center frequency of the transmitted pulse. Focusing on the $R - v_\mathrm{d}$ space, the discrete points, defined as $\boldsymbol{\zeta}^{(m,n)} \equiv (\tilde{R}^{(m,n)}, v_\mathrm{d}^{(m,n)})$, can be extracted from the local maxima of $S(\boldsymbol{r}_\mathrm{T}, \boldsymbol{r}_\mathrm{R}, R, v_\mathrm{d}; \tau_m)$ as:

$$\left.\begin{array}{l} \partial|S(\boldsymbol{r}_\mathrm{T}, \boldsymbol{r}_\mathrm{R}, R, v_\mathrm{d}; \tau_m)|/\partial R = 0 \\ \partial|S(\boldsymbol{r}_\mathrm{T}, \boldsymbol{r}_\mathrm{R}, R, v_\mathrm{d}; \tau_m)|/\partial v_\mathrm{d} = 0 \\ |S(\boldsymbol{r}_\mathrm{T}, \boldsymbol{r}_\mathrm{R}, R, v_\mathrm{d}; \tau_m)| \geq \alpha \max_{(R,v_\mathrm{d})} |S(\boldsymbol{r}_\mathrm{T}, \boldsymbol{r}_\mathrm{R}, R, v_\mathrm{d}; \tau_m)| \end{array}\right\}.$$

where α is the threshold parameter with $0 \leq \alpha \leq 1$ and n denotes the index number of the local maxima. By using the following filtering process in the R-v_d space, the Doppler decomposed data for each $\boldsymbol{\zeta}^{(m,n)}$ is obtained as:

$$\tilde{s}(\boldsymbol{r}_\mathrm{T}, \boldsymbol{r}_\mathrm{R}, R, \tau; \boldsymbol{\zeta}^{(m,n)})$$
$$= \frac{1}{2\pi} \int W(R, v_\mathrm{d}; \boldsymbol{\zeta}^{(m,n)})S(\boldsymbol{r}_\mathrm{T}, \boldsymbol{r}_\mathrm{R}, R, v_\mathrm{d}; \tau_m)e^{j\omega\tau}d\omega. \tag{2}$$

where $W(R, v_\mathrm{d}; \boldsymbol{\zeta}^{(m,n)})$ is the windowing filter in the R-v_d space.

Then, for the n-th clustered data as $\tilde{s}(\boldsymbol{r}_\mathrm{T}, \boldsymbol{r}_\mathrm{R}, R, \tau; \boldsymbol{\zeta}^{(m,n)})$, the coherent integration (CI) based radar imaging process is applied, to provide the v_d associated radar image [22] as :

$$I(\boldsymbol{r}, \tau; \boldsymbol{\zeta}^{(m,n)}) = \sum_{\boldsymbol{r}_\mathrm{T}, \boldsymbol{r}_\mathrm{R}} w(\boldsymbol{r}_\mathrm{T}, \boldsymbol{r}_\mathrm{R})$$
$$\times \int_{-\infty}^{\infty} \tilde{S}(\boldsymbol{r}_\mathrm{T}, \boldsymbol{r}_\mathrm{R}, \omega, \tau; \boldsymbol{\zeta}^{(m,n)})G_\mathrm{R}^*(\omega, \boldsymbol{r}, \boldsymbol{r}_\mathrm{R})G_\mathrm{T}^*(\omega; \boldsymbol{r}_\mathrm{T}, \boldsymbol{r})d\omega \tag{3}$$

where $\tilde{S}(\boldsymbol{r}_\mathrm{T}, \boldsymbol{r}_\mathrm{R}, \omega, \tau; \boldsymbol{\zeta}^{(m,n)})$ denotes the 1D FT of $\tilde{s}(\boldsymbol{r}_\mathrm{T}, \boldsymbol{r}_\mathrm{R}, R, \tau; \boldsymbol{\zeta}^{(m,n)})$ in terms of t via the relationship of $t = 2R/\mathrm{c}$. Here, $G_\mathrm{T}(\omega; \boldsymbol{r}_\mathrm{T}, \boldsymbol{r})$ and $G_\mathrm{R}(\omega, \boldsymbol{r}, \boldsymbol{r}_\mathrm{R})$ denote the Green's functions defined as from the transmitter position $\boldsymbol{r}_\mathrm{T}$ to the imaging point $\boldsymbol{r}$ and the imaging point $\boldsymbol{r}$ to the receiver position $\boldsymbol{r}_\mathrm{R}$, respectively. Under the condition of a homogeneous background, these Green's functions are expressed as: $G_\mathrm{T}(\omega; \boldsymbol{r}_\mathrm{T}, \boldsymbol{r}) \simeq \exp\left(j\frac{\omega}{c_\mathrm{B}}\|\boldsymbol{r} - \boldsymbol{r}_\mathrm{T}\|\right)$ and $G_\mathrm{R}(\omega; \boldsymbol{r}, \boldsymbol{r}_\mathrm{R}) \simeq \exp\left(j\frac{\omega}{c_\mathrm{B}}\|\boldsymbol{r}_\mathrm{R} - \boldsymbol{r}\|\right)$, where c_B denotes the propagation speed in the air. Notably, $w(\boldsymbol{r}_\mathrm{T}, \boldsymbol{r}_\mathrm{R})$ is the weight term for the element location, which is expressed as:

$$w(\boldsymbol{r}_\mathrm{T}, \boldsymbol{r}_\mathrm{R}) = \exp\left\{-\frac{\|\boldsymbol{r}(\boldsymbol{r}_\mathrm{T}, \boldsymbol{r}_\mathrm{R}) - \boldsymbol{r}_\mathrm{C}\|^2}{2\sigma_\mathrm{array}^2}\right\} \tag{4}$$

where $\boldsymbol{r}_\mathrm{C}$ is the center location of the equivalent array. Here, σ_array is set to an aperture length for an equivalent array, and the weight term $w(\boldsymbol{r}_\mathrm{T}, \boldsymbol{r}_\mathrm{R}$ suppresses the sidelobe effect in radar imaging, although its cross-range resolution is reduced.
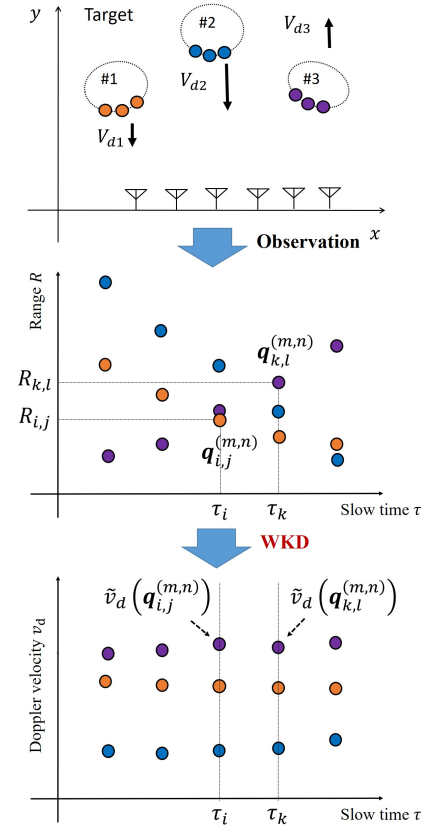

Fig. 2: Doppler estimation scheme using WKD method.

This method [22] realizes a high spatial resolution and v_d associated radar imaging, which contributes to multifunctional imaging for complex shaped and partially moving objects, *e.g.*, pedestrians and cyclists. However, the associated Doppler velocity v_d is determined by the STFT given in Eq. (1); thus, there is a trade-off between the temporal and velocity resolution, and there is an inherent limitation in terms of the unambiguous velocity range determined by the Nyquist criteria. In particular, assuming a human walking model, the velocity range required to track each body part (*e.g.*, legs or arms) should exceed 2.0 m/s. This, for example, necessitates a PRI of less than 0.5 ms when using a 79-GHz band MMW radar. However, achieving such PRI levels is challenging in general MIMO MMW radar models, as because the number of pulse sequences for each transmitting pulse increases the lower boundary of the PRI. In addition, the obtained Doppler velocity is averaged over the CPI, *i.e.*, the temporal resolution, and cannot track velocity changes during the CPI, which is critical for tracking each part with pendulum motion in the walking model. Note that these limitations have been demonstrated or discussed in the literature [22].

C. Proposed Doppler Velocity Associated Radar Imaging

1) Weighted Kernel Density Estimation (WKD) Method: To address the aforementioned problem, the proposed method integrates the WKD-based Doppler velocity estimation [23]
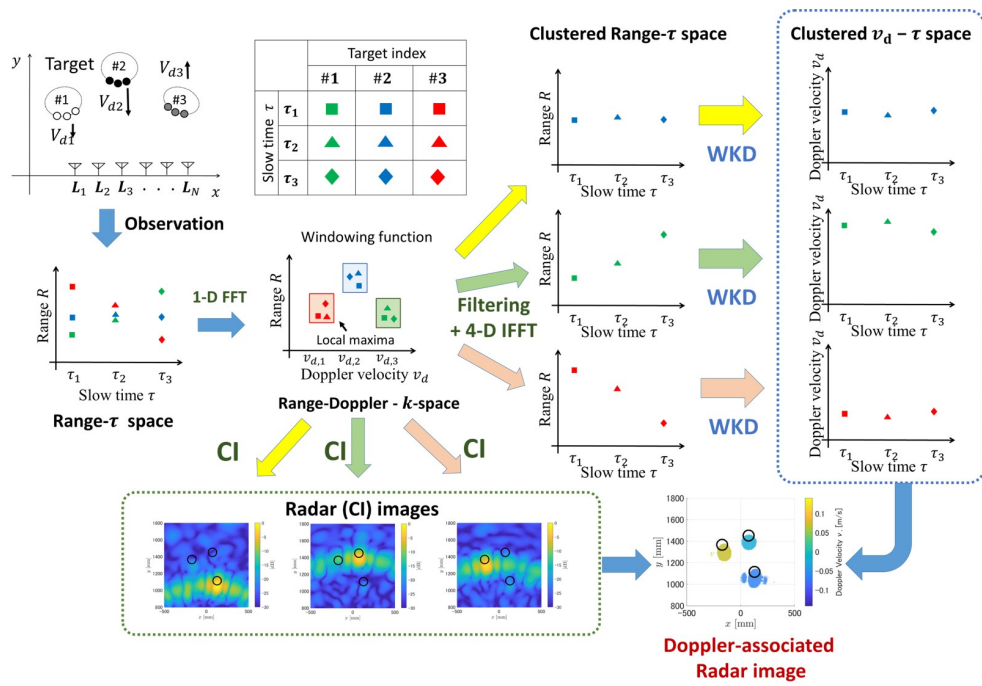
Fig. 3: Schematic diagram of the proposed method.

with the v_d decomposed radar image $I(\boldsymbol{r}, \tau; \boldsymbol{\zeta}^{(m,n)})$. First, we provide a brief overview of the WKD methodology. The WKD method leverages an incoherent transformation from the TOF point cloud data to the associated Doppler velocity and effectively addresses the limitations inherent in Fourier-based Doppler analysis. Here, we define the range-τ points as $\boldsymbol{q}_{i,j}^{(m,n)} \equiv (\boldsymbol{r}_{\mathrm{T},i,j}^{(m,n)}, \boldsymbol{r}_{\mathrm{R},i,j}^{(m,n)}, R_{i,j}^{(m,n)}, \tau_j^{(m,n)})$, which are extracted from the local maxima of the v_d decomposed data $|\tilde{s}(\boldsymbol{r}_\mathrm{T}, \boldsymbol{r}_\mathrm{R}, R, \tau; \boldsymbol{\zeta}^{(m,n)})|$ as:

$$\frac{\partial |\tilde{s}(\boldsymbol{r}_\mathrm{T}, \boldsymbol{r}_\mathrm{R}, R, \tau; \boldsymbol{\zeta}^{(m,n)})|}{\partial R} = 0 \tag{5}$$

$$|\tilde{s}(\boldsymbol{r}_\mathrm{T}, \boldsymbol{r}_\mathrm{R}, R, \tau; \boldsymbol{\zeta}^{(m,n)})| \geq \beta \max_{R,\tau} |\tilde{s}(\boldsymbol{r}_\mathrm{T}, \boldsymbol{r}_\mathrm{R}, R, \tau; \boldsymbol{\zeta}^{(m,n)})| \tag{6}$$

where β expresses the threshold with $0 \leq \beta \leq 1$. Here, in the definition of $\boldsymbol{q}_{i,j}^{(m,n)}$, the subscript i represents the i-th slow time snapshot at τ_i, the subscript j expresses the index number of the extracted range-τ points at each τ_i, and the superscript (m,n) denotes that it belongs to the n-th cluster in the v_d decomposition process in the m-th CPI.

Focusing on the inclination value between the two range-τ points denoted as $\boldsymbol{q}_{i,j}^{(m,n)}$ and $\boldsymbol{q}_{k,l}^{(m,n)}$, an instantaneous Doppler velocity is incoherently defined as $v_\mathrm{d}(\boldsymbol{q}_{i,j}^{(m,n)}, \boldsymbol{q}_{k,l}^{(m,n)}) \equiv (R_{i,j}^{(m,n)} - R_{k,l}^{(m,n)})/(\tau_i^{(m,n)} - \tau_k^{(m,n)})$. Using some of these possible Doppler velocities $v_\mathrm{d}(\boldsymbol{q}_{i,j}^{(m,n)})$, the optimal Doppler velocity for the focused range-τ point

as $\boldsymbol{q}_{i,j}^{(m,n)}$ is determined as:

$$\tilde{v}_\mathrm{d}(\boldsymbol{q}_{i,j}^{(m,n)}) = \arg \max_{v_\mathrm{d}} \sum_{k,l} \exp\left(-\frac{\left||\tilde{s}(\boldsymbol{q}_{i,j}^{(m,n)})| - |\tilde{s}(\boldsymbol{q}_{k,l}^{(m,n)})|\right|^2}{2\sigma_s^2}\right)$$

$$\times \exp\left(-\frac{|\tau_i - \tau_k|^2}{2\sigma_\tau^2}\right) \exp\left(-\frac{|v_d - v_\mathrm{d}(\boldsymbol{q}_{i,j}^{(m,n)}, \boldsymbol{q}_{k,l}^{(m,n)})|^2}{2\sigma_{v_d}^2}\right), \tag{7}$$

where $|\tilde{s}(\boldsymbol{q}_{i,j}^{(m,n)})|$ expresses the signal strength, namely, $|\tilde{s}(\boldsymbol{r}_\mathrm{T}, \boldsymbol{r}_\mathrm{R}, R_i, \tau_j; \boldsymbol{\zeta}^{(m,n)})|$. In addition, σ_s, σ_τ, and σ_{v_d} are constants, and their roles are described in detail in the literature [23].

The WKD has a notable advantage in that the optimized Doppler velocity $\tilde{v}_\mathrm{d}(\boldsymbol{q}_{i,j}^{(m,n)})$ can be provided at each slow time τ_i, which means that the temporal resolution of WKD is identical to that of the PRI. In addition, as a candidate, the Doppler velocity is determined via an inclination by a possible combination of range-τ points as $v_\mathrm{d}(\boldsymbol{q}_{i,j}^{(m,n)}, \boldsymbol{q}_{k,l}^{(m,n)})$, $v_\mathrm{d}(\boldsymbol{q}_{i,j}^{(m,n)}, \boldsymbol{q}_{k,l}^{(m,n)})$, and there is no limitation in terms of the velocity resolution and the unambiguous velocity range, that has been demonstrated in [23]. Notably, although the WKD method could be integrated into the RPM-based imaging scheme, the RPM cannot retain sufficient angular resolution in the MMW band, such as at 79 GHz, due to incoherent processing.

2) Integration WKD and CI: To integrate a high-resolution Doppler-decomposed CI image with a WKD-based Doppler estimator, this study introduces a novel integration scheme for combining CI imaging with the WKD method as follows. The WKD method provides point cloud outputs denoted as $\tilde{v}_\mathrm{d}(\boldsymbol{q}_{i,j}^{(m,n)})$, which needs to be effectively associated with the synthesized, distributed CI image. To achieve this association,

the most reliable Doppler velocity is selected from all the available points $\tilde{v}_{\mathrm{d}}(\boldsymbol{q}_{i,j}^{(m,n)})$ within the cluster $\boldsymbol{\zeta}^{(m,n)}$. Specifically, the WKD point cloud data, $\tilde{v}_{\mathrm{d}}(\boldsymbol{q}_{i,j}^{(m,n)})$, and the v_{d} decomposed radar image as $I(\boldsymbol{r}, \tau; \boldsymbol{\zeta}^{(m,n)})$ are integrated via the cluster vector $\boldsymbol{\zeta}^{(m,n)}$. The representative Doppler velocity $\hat{v}_{\mathrm{d}}^{(m,n)}$ for each cluster is derived from $\boldsymbol{\zeta}^{(m,n)}$ as

$$\hat{v}_{\mathrm{d}}^{(m,n)} = \tilde{v}_{\mathrm{d}}(\hat{\boldsymbol{q}}^{(m,n)}) \tag{8}$$

$$\hat{\boldsymbol{q}}^{(m,n)} = \arg \max_{\boldsymbol{q}_{i,j}^{(m,n)}} F\left(\boldsymbol{q}_{i,j}^{(m,n)}\right) \tag{9}$$

where $F\left(\boldsymbol{q}_{i,j}^{(m,n)}\right)$ denotes the maximized evaluation function for $\boldsymbol{q}_{i,j}^{(m,n)}$, *i.e.*, the left hand side of Eq. (7). Then, the Doppler velocity decomposed radar image in Eq. (3) is updated as $I(\boldsymbol{r}, \tau; \hat{v}_{\mathrm{d}}^{(m,n)})$ using the WKD determined $\hat{v}_{\mathrm{d}}^{(m,n)}$). It is worth noting that this method offers a distinct advantage as the high-resolution CI radar image can be seamlessly integrated with the ambiguity-free Doppler velocity estimation obtained from the WKD. This approach effectively combines the strengths of coherent (STFT) and incoherent (WKD) processes. Even if aliasing effect occurs in the STFT based Doppler decomposition, it does not affect the post-WKD-based velocity estimation, as the WKD itself relies only on the magnitude of the range-τ responses, expressed as $|\tilde{s}(\boldsymbol{q}_{i,j}^{(m,n)})|$. This capability addresses a fundamental limitation of the conventional STFT-based approach [22]. Furthermore, by analyzing the point cloud $\tilde{v}_{\mathrm{d}}(\boldsymbol{q}_{i,j}^{(m,n)})$ within $\boldsymbol{\zeta}^{(m,n)}$, we can examine the temporal variations of the Doppler velocity within the CPI. This is possible because the WKD provides instantaneous Doppler velocity measurements for each pulse hit, allowing the temporal resolution to be reduced to a single PRI. Figure 3 presents a conceptual diagram that illustrates the proposed method, where the point cloud outputs of the WKD are associated with the radar images for each cluster $\boldsymbol{\zeta}^{(m,n)}$.

3) Processing Flow of Proposed Method : The detailed procedure of the proposed method is described as follows:

Step 1): The received signals $s(\boldsymbol{r}_{\mathrm{T}}, \boldsymbol{r}_{\mathrm{R}}, R, \tau)$ are processed by a matched filter as $\tilde{s}(\boldsymbol{r}_{\mathrm{T}}, \boldsymbol{r}_{\mathrm{R}}, R, \tau)$.

Step 2): $\tilde{s}(\boldsymbol{r}_{\mathrm{T}}, \boldsymbol{r}_{\mathrm{R}}, R, \tau)$ is then truncated with a certain CPI as T at the center slow time τ_m, and $\tilde{s}(\boldsymbol{r}_{\mathrm{T}}, \boldsymbol{r}_{\mathrm{R}}, R, \tau; \tau_m)$ is obtained.

Step 3): $S(\boldsymbol{r}_{\mathrm{T}}, \boldsymbol{r}_{\mathrm{R}}, R, v_{\mathrm{d}}; \tau_m)$ is calculated by applying the 1D DFT to $\tilde{s}(\boldsymbol{r}_{\mathrm{T}}, \boldsymbol{r}_{\mathrm{R}}, R, \tau; \tau_m)$ using Eq. (1).

Step 4): $\boldsymbol{\zeta}^{(m,n)}$ is extracted from the local maxima of $|S(\boldsymbol{r}_{\mathrm{T}}, \boldsymbol{r}_{\mathrm{R}}, R, v_{\mathrm{d}}; \tau_m)|$ using Eq. (2), and its inverse Fourier transform $\tilde{s}(\boldsymbol{r}_{\mathrm{T}}, \boldsymbol{r}_{\mathrm{R}}, R, \tau; \boldsymbol{\zeta}^{(m,n)})$ is calculated in Eq. (2).

Step 5): For the n-th cluster in the m-th CPI, the range-τ points $\boldsymbol{q}_{i,j}^{(m,n)}$ are extracted using Eq. (6).

Step 6): Focusing on the specific range-τ point as $\boldsymbol{q}_{i,j}^{(m,n)}$, the optimal Doppler velocity $\tilde{v}_{\mathrm{d}}(\boldsymbol{q}_{i,j}^{(m,n)})$ is obtained
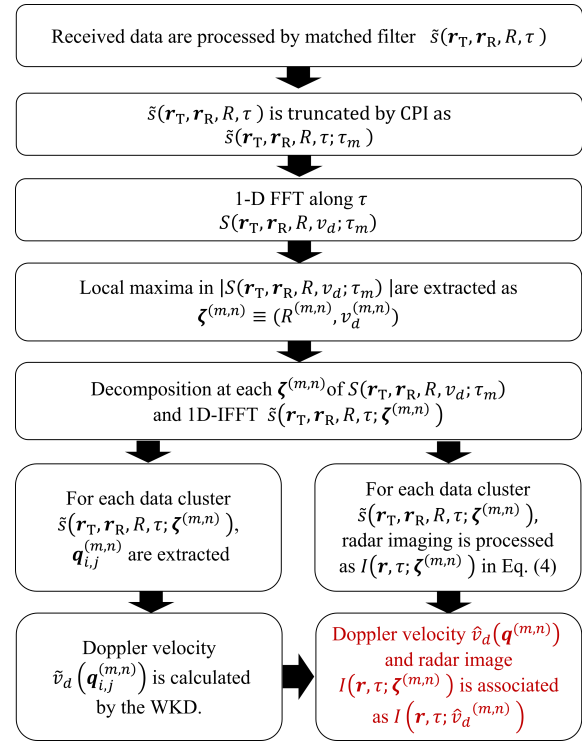

Fig. 4: Flowchart of the proposed method.

using the WKD method as given in Eq. (7).

Step 7) : Radar imaging processing in Eq. (3) is applied to each cluster data $\tilde{s}(\boldsymbol{r}_{\mathrm{T}}, \boldsymbol{r}_{\mathrm{R}}, R, \tau; \boldsymbol{\zeta}^{(m,n)})$. In addition, a representative Doppler velocity $\hat{v}_{\mathrm{d}}^{(m,n)}$ is determined using Eq. (9), which is obtained as the Doppler associated radar image as $I(\boldsymbol{r}, \tau; \hat{v}_{\mathrm{d}}^{(m,n)})$.

Step 8) : τ_m is changed to τ_{m+1} and the Steps 2) to 7) are repeated.

Step 9) : $I(\boldsymbol{r}, \tau; \hat{v}_{\mathrm{d}}^{(m,n)})$ are calculated for all τ_m.

In each CPI, the proposed method generates n different radar images as $I(\boldsymbol{r}, \tau; \hat{v}_{\mathrm{d}}^{(m,n)})$, which are associated with different Doppler velocities $\hat{v}_{\mathrm{d}}^{(m,n)}$. Fig. 4 shows a flowchart of the proposed method.

III. RESULTS

A. Experimental Setting

The proposed method was validated experimentally. In this evaluation, a radar module with a 79-GHz band FMCW MIMO radar device (produced by Sakura Tech Corp) with 4.0 GHz bandwidth (37.5 mm range resolution) acquired data with pulse sequences, as shown in Fig. 5. Here, six transmitters (output power: 10 dBm) and eight receivers were used to configure a planar MIMO array, where its center position, defined as the origin $(x, y, z) = (0, 0, 0)$, was set to 715 mm above the floor. The antenna beam widths that defined the field of view, were $\pm 10°$ and $\pm 45°$ for the vertical and horizontal axes, respectively. This configuration was chosen to enable 2-D cross-sectional imaging on the azimuth plane, as determined by the radar height ($z = 715$

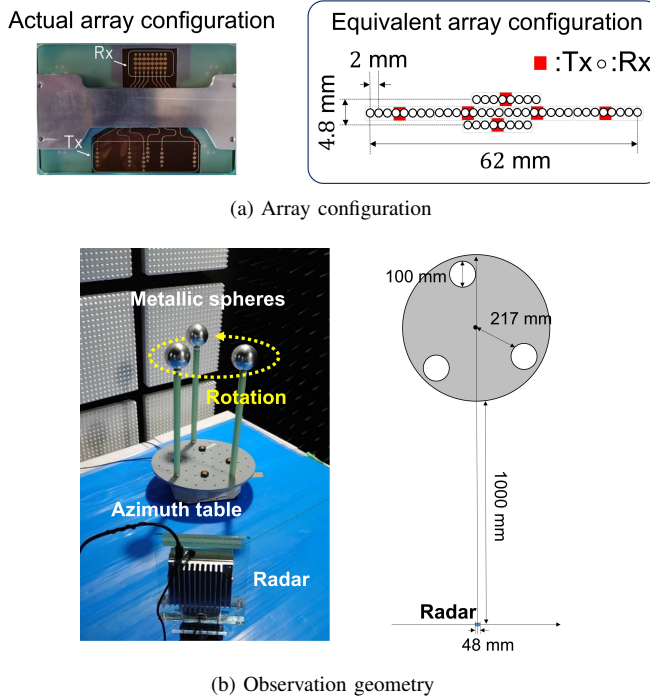(a) Array configuration

(b) Observation geometry

Fig. 5: Experimental setup in rotating spheres model.

mm). Thus, the radar receives reflection echoes exclusively from the region that is at the same height as the radar, effectively suppressing clutter that originates from different heights. The real and virtual array arrangement is shown in Fig. 5, where the horizontal and vertical dimensions of the equivalent array were 62 mm and 4.8 mm, respectively, *i.e.*, the azimuth and elevation angular resolutions were 1.82 and 44.68 degrees, respectively. Note that the vertical beam width was narrowed sufficiently (*i.e.*, 10 degrees), and the target was located at a distance of approximately 1 m; thus, we extracted the cross-sectional image of $I(\boldsymbol{r}, \tau; \hat{v}_{\mathrm{d}}^{(m,n)})$ at a radar height of approximately $-100\mathrm{mm} \leq z \leq 100\mathrm{mm}$, thereby representing a quasi-2D imaging problem.

B. Case for Rotating Three Metallic Spheres

First, an experimental case involving the rotation of multiple spheres was investigated. This simplified object model allowed us to evaluate the localization or velocity estimation errors in the quantitative mean. Fig. 5-(b) shows the observation geometry used in this case. The three metallic spheres with 100-mm diameter were rotated with a radius of 217 mm. The center of these spheres was set to a height of 790 mm, which is nearly the same as that of the MMW radar (715 mm), and the rotation center was set to 1,250 mm from the radar device. In addition, a stop and go observation technique was employed to acquire a reliable ground truth profile in terms of both the location and velocity. In this case, the PRI was 7 ms, which determined an unambiguous velocity range of ± 0.141 m/s, Note that this velocity range is smaller than the maximum Doppler velocity of each sphere of 0.20 m/s. The total number of all pulse sequences was 570, which means that the total observation time was 3.99 s. Here, the CPI (*i.e.*, the temporal resolution) was set to

0.399 s (57 pulse hits) in the STFT-based Doppler velocity decomposition given in Eq. (1), which indicates a velocity resolution of 4.94×10^{-3} m/s.

Fig. 6 (a) - (e) illustrates the ground truth profiles, where each color denotes the Doppler velocity at the center of CPI, and Fig. 6 (f)-(j) denote the conventional CI image, *i.e.*, without Doppler velocity decomposition process. Furthermore, Fig. 6 (k)-(o) show the range-Doppler profiles obtained using the Step 3) of the proposed method, Figures 6 (p)-(t) and Figures 6 (u)-(y) illustrate the reconstruction images obtained by the method [22] and the proposed method, respectively, where each reconstruction image is binarized by a constant threshold (0.2 times greater than the maximum response) and is associated with the Doppler velocity (with color) obtained by using the STFT or WKD method, respectively. Here, the weighting parameter σ_{array} in Eq. (4) was set to 15 mm in both methods, which is one-quarter of the array aperture, and $\alpha = 0.1$ was set in Eq. (2) The WKD parameters were set to $\beta = 0.1$ for Eq. (6), and $\sigma_\tau = 0.04$ s, $\sigma_{\mathrm{s}} = 0.7$ and $\sigma_{v_{\mathrm{d}}} = 0.2$ m/s were set for Eq. (7). As shown in the results obtained by the traditional CI images in Fig. 6 (f) - (j), the two or three responses are clearly separated in the reconstruction, which indicates that a sufficient azimuth angle resolution was available in this case. In addition, the range-Doppler profiles shown in Fig. 6 (k)-(o) validate that the Doppler velocity resolution was sufficiently high to resolve each target response along the Doppler velocity direction. However, the associated images shown in Fig. 6 (p)-(t), namely, $I(\boldsymbol{r}, \tau; \boldsymbol{\zeta}^{(m,n)})$ in Eq. (3) are simply associated with the $v_{\mathrm{d}}^{(m,n)}$ obtained via the STFT analysis as [22], thus, it could not provide an accurate estimation, due to a limited unambiguous velocity range (± 0.141 m/s). In contrast, the proposed association images shown in Fig. 6 (u)-(y) exhibit more accurate Doppler velocity estimation, because the WKD Doppler estimator is free of the maximum velocity limitation, and the Doppler velocity with the maximum evaluation value in Eq. (7) provides the most reliable estimation among the other range-Doppler points, in each CPI period. For reference, Fig. 7 shows the Doppler estimation results obtained by the WKD method. As can be seen, the WKD method generated an accurate Doppler velocity for all three objects, and its Doppler velocity varied considerably in each CPI period. These results demonstrate that the WKD method retains much higher temporal resolution and accurate Doppler velocity estimation, which could not be obtained using the STFT-based analysis. In addition, Fig. 8 compares the errors in the velocity estimations for the method [22] and the proposed method. These results demonstrate that the proposed scheme (*i.e.*, WKD-based estimation) offers significant improvement over all CPIs. In particular, the comparison of the average values of these errors shows that the proposed method (0.183 m/s) achieves velocity estimations four times more accurate than those obtained using the method in [22] (0.720 m/s).

This article has been accepted for publication in IEEE Sensors Journal. This is the author's version which has not been fully edited and content may change prior to final publication. Citation information: DOI 10.1109/JSEN.2025.3547312

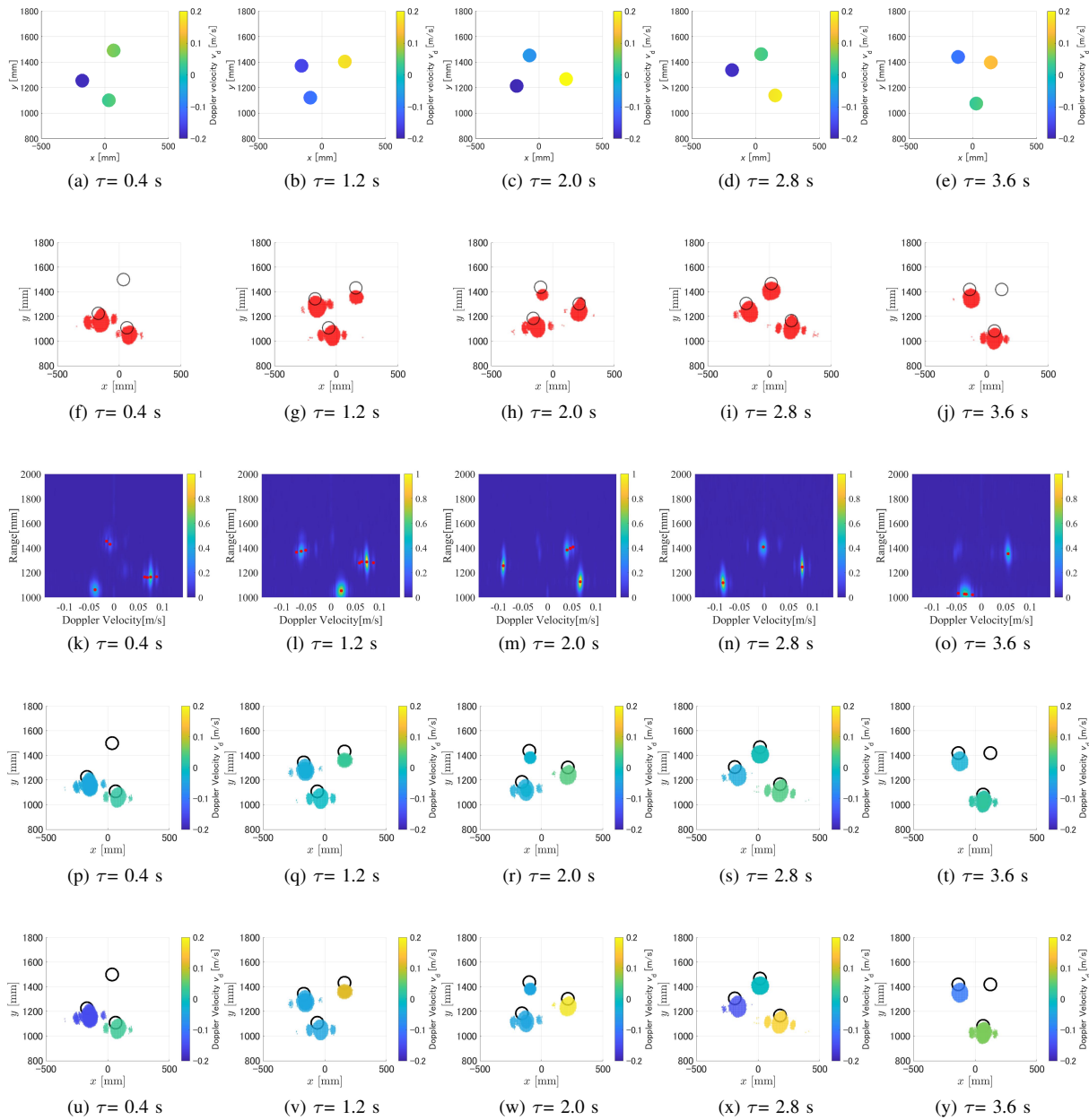Y. SEKIGAWA *et al.*: DOPPLER ASSOCIATED 79 GHZ BAND MMW RADAR IMAGING 7

Fig. 6: Results at each slow time in three rotating spheres model. 1st row: Ground truth profiles. 2nd row : Reconstructions w/o Doppler velocity decomposition. 3rd row : Range-v_d profiles. 4th row : Reconstructions w/ Doppler velocity decomposition (STFT) in [22]. 5th row: Reconstructions w/ Doppler velocity decomposition (WKD). Red dots in (k), (l), (m), (n), and (o) denote the extracted local maxima. Colors in from (p) to (y) denote the Doppler velocity.

C. Case for Real Walking Human

The proposed method was also evaluated using the case of a walking human. Here, the human subject (height: 178 cm) was positioned 1.5 m from the radar site, and the subject performed a stepping periodic motion with a period of approximately 1.3 s. Thus, with the radar height set at 715 mm, the reflected signals are expected to primarily capture echoes from the upper legs, lower arms, and torso regions. The PRI is set to 7 ms, and the total number of all pulse sequences was 380, which means that the total observation time was 2.66 s. The CPI is set to 0.133 s (19 pulse hits) in the STFT-based Doppler velocity decomposition [22], indicating a velocity resolution of 1.48×10^{-2} m/s. To introduce quantitative error analysis, a simplified walking model with 11 ellipsoids was introduced, comprising the upper and lower arms, the legs, the torso, and the head. By considering the actual motions in the optical video, the rotation and translation motions for each part were given by the pendulum model. These simplified numerical models provide referential location and time-varying motion vectors,
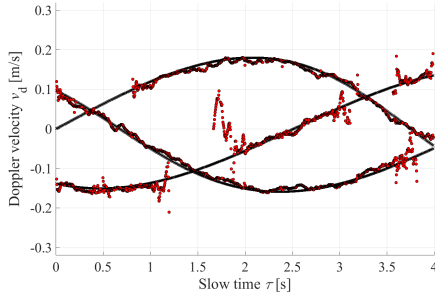
Fig. 7: Doppler velocity estimation results by the WKD method in three rotating spheres model. Black curve: Ground truth. Red dots: Estimated by the WKD.
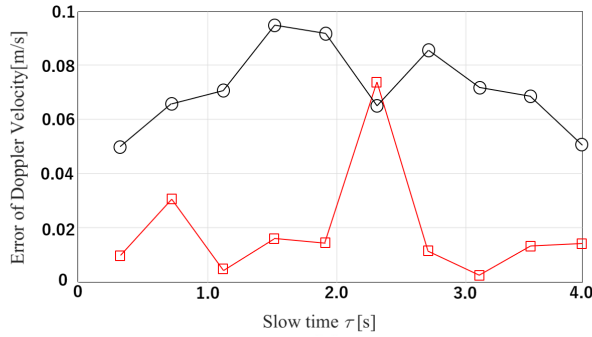

Fig. 8: Errors in Doppler velocity estimation in each slow time for three rotating spheres model. Black dots: STFT [22]. Red dots: WKD.

including Doppler velocity, at each slow time. Fig. 9 shows the experimental model with a walking human body and the numerical human model (11 ellipsoids) with representative snapshots along the slow time, which are considered the ground truth profiles of the target locations and velocities. Fig. 10 (a) - (e) illustrates the ground truth profiles at each center of CPI, where colors denote the Doppler velocity value, and Fig. 10 (f)-(j) denote the conventional CI image, *i.e.*, without Doppler velocity decomposition process. Fig. 10 (k)-(o) show the range-Doppler profiles, and Fig. 10 (p)-(y) also present the reconstruction results by each method, where the parameters of α, β, σ_{array}, σ_{s}, σ_{τ}, and $\sigma_{v_{\text{d}}}$ were set as described in Section III-B. For the results obtained by the original CI (Fig. 10 (f)-(j)), while there are some unnecessary responses that deviated from the actual shape, and some parts of the body, *e.g.*, the arms or legs, could be reconstructed in the original CI. Focusing on the range-Doppler profile in Fig. 10 (k)-(o), dominant responses can be observed in the range of 1550 mm, and these were primarily caused by torso parts, and some responses around $1000 \text{ m} \leq R \leq 1200 \text{ m}$ could also be extracted as local maxima, which were caused by a raised arm or leg with large motion. However, in the method [22], since the maximum velocity range ± 0.141 m/s is considerably smaller than the actual velocity caused by the walking motion over 2.0 m/s; thus, the extracted Doppler velocities in the STFT based range-Doppler profiles could not offer an accurate Doppler associated radar image (Fig. 10 (p)-(t)). Focusing on the Doppler associated image shown in Fig. 10 (u)-(y) obtained using the WKD based Doppler

(a) Optical images
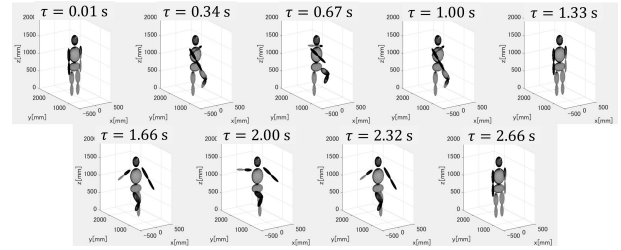
(b) Numerical models

Fig. 9: Walking human model in the experiment.

association, we can see that some unnecessary responses in the conventional CI (in Fig. 10 (h) and (i)) could be suppressed by filtering the Doppler space, and each Doppler velocity could be estimated over 0.5 m/s. Fig. 12 shows the quantitative error analysis of the Doppler velocity estimation for each CPI sequence, and the results demonstrate that the proposed method retained more accurate Doppler velocities for nearly all CPI sequences.

Finally, we investigate the computational complexity and run-time required for each method, where Intel Xeon Gold 6330 CPU 2.0 GHz with 2 TB RAM is used in all cases. Table I summarizes these metrics for the three methods: the original DAS method (without Doppler decomposition), the method proposed in [22], and our proposed method. Key notations include N_{T} and N_{R} which represent the number of transmitters and receivers, respectively, and N_t the sampling number along the fast-time t. N_x and N_y the number of pixels in the radar image along the x and y axes, respectively. N_{CPI} and N_{cluster} correspond to the number of CPI (T) in Eq. (1) and the number of clusters denoted as $\boldsymbol{\zeta}^{(m,n)}$, respectively. Also, N_{RP} denotes the number of Range-τ point in each cluster. n both the original and proposed methods, the parameters are fixed as follows: $N_{\text{T}} = 4$, $N_{\text{R}} = 8$, $N_x = 1000$, $N_y = 600$, $N_t = 15800$ and $N_{\text{CPI}} = 19$ while N_{cluster} and N_{RP} vary depending on the target case. Notably, in the method [22], Step 6 is not required, although other parameters, such as N_{cluster} or N_{CPI} remain consistent with the proposed method. This table reveals that Step 2, 3, 4, and 5 account for 99.1 % of the total computation time (1871 s). This computational demand is nearly identical in both the method described in [22] and our proposed method, as both require STFT-based Doppler velocity decomposition and clustering. While the total processing time for both the previous and the proposed methods is approximately 30 minutes, the additional computational cost of the proposed method (Step 6: WKD related process) is only 7 s, accounting for approximately 0.4 % of the total runtime. Thus, the proposed method addresses a critical limitation in STFT-

(a) τ= 0.20 s   (b) τ= 0.47 s   (c) τ= 0.60 s   (d) τ= 1.40 s   (e) τ= 2.60 s

(f) τ= 0.20 s   (g) τ= 0.47 s   (h) τ= 0.60 s   (i) τ= 1.40 s   (j) τ= 2.60 s

(k) τ= 0.20 s   (l) τ= 0.47 s   (m) τ= 0.60 s   (n) τ= 1.40 s   (o) τ= 2.60 s

(p) τ= 0.20 s   (q) τ= 0.47 s   (r) τ= 0.60 s   (s) τ= 1.40 s   (t) τ= 2.60 s

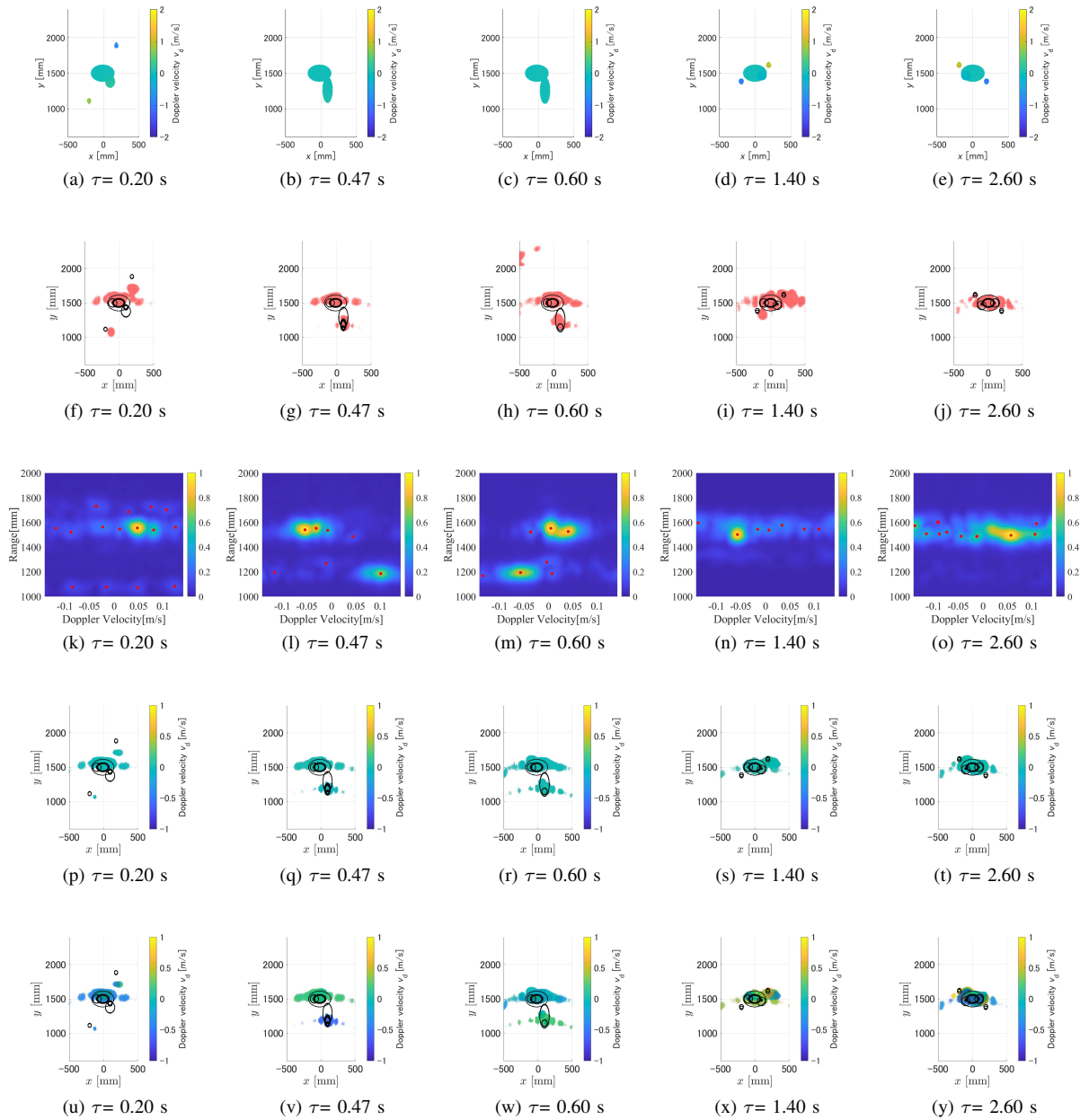(u) τ= 0.20 s   (v) τ= 0.47 s   (w) τ= 0.60 s   (x) τ= 1.40 s   (y) τ= 2.60 s

Fig. 10: Results obtained by each method at different slow times. 1st row: Ground truth profiles. 2nd row : Reconstructions w/o Doppler velocity decomposition. 3rd row : Range-v_{d} profiles. 4th row : Reconstructions w/ Doppler velocity decomposition (STFT) in [22]. 5th row: Reconstructions w/ Doppler velocity decomposition (WKD). Red dots in (k), (l), (m), (n), and (o) denote the extracted local maxima. Black ellipsoids in the image denotes the cross-sectional images at $z = -100, 0,$ and 100 mm. Colors in from (p) to (y) denote the Doppler velocity.

based Doppler estimation while incurring minimal additional computational cost, maintaining a complexity comparable to that of the method in [22]. This advantage highlights the efficiency and precision of our approach.

Notably, because the field of view of this radar module is significantly limited to the elevation angle, different cross-sectional images can be obtained by adjusting the radar height. This adjustment also effectively suppresses clutter signals that originate from different heights, such as from the ground or a road surfaces. Additionally, even in scenarios

where multiple pedestrians are present within the field of view, the proposed scheme retains a distinct advantage over the conventional STFT-based scheme [22]. This is because the high range resolution achievable in the 79 GHz band (*e.g.*, 37.5 mm) allows for the effective decomposition of multiple pedestrians along the range axis. Even when multiple individuals are located within the same range resolution cell (*i.e.*, within 37.5 mm), the 79 GHz band MIMO radar provides sufficient angular resolution to differentiate between multiple human bodies. For example, at a distance of 10 m,

TABLE I: Computational complexity and actual run time in each τ.

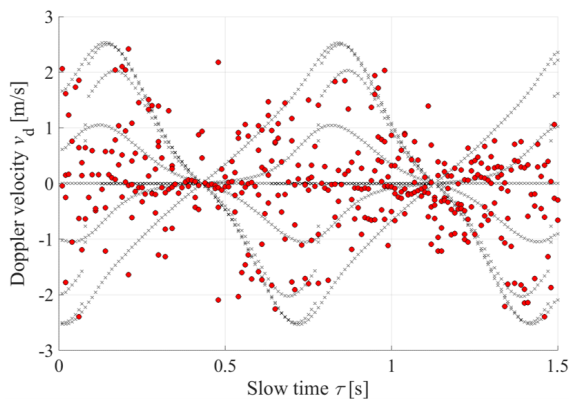| Method	Step	Complexity	Run time
Original DAS	1	$O(N_{\mathrm{T}} N_{\mathrm{R}} N_{\mathrm{CPI}} N_t \log N_t)$	3.0 s
	7	$O(N_{\mathrm{T}} N_{\mathrm{R}} N_x N_y)$	6.8 s
	Total		9.8 s
	1	$O(N_{\mathrm{T}} N_{\mathrm{R}} N_{\mathrm{CPI}} N_t \log N_t)$	3.0 s
Method [22]	2,3	$O(N_{\mathrm{T}} N_{\mathrm{R}} N_{\mathrm{CPI}} \log N_{\mathrm{CPI}})$	84 s
(except for Step 6)	4,5	$O(N_{\mathrm{T}} N_{\mathrm{R}} N_{\mathrm{cluster}} N_{\mathrm{CPI}} \log N_{\mathrm{CPI}})$	1770 s
Proposed	6	$O(N_{\mathrm{T}} N_{\mathrm{R}} N_{\mathrm{cluster}} N_{\mathrm{RP}})$	7.0 s
	7	$O(N_{\mathrm{T}} N_{\mathrm{R}} N_x N_y N_{\mathrm{cluster}})$	6.8 s
Method [22]	Total		1863.8 s
Proposed	Total		1870.8 s

Fig. 11: Doppler velocity estimation results by the WKD method in walking human model. Black curve: Ground truth. Red dots: Estimated by the WKD.
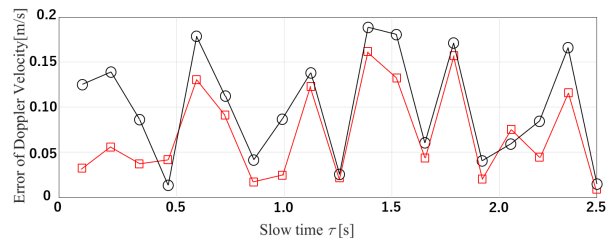

Fig. 12: Errors in Doppler velocity estimation in each slow time in walking human model. Black dots: STFT [22]. Red dots: WKD.

the radar achieves an azimuth resolution of 310 mm, which is significantly smaller than the average human body width (approximately 600 mm). This feature is also retained in the conventional STFT based scheme. However, it is unable to retain a sufficient Doppler velocity range, which is a critical limitation in accurately measuring the relative speed of the target motion and vehicles.

IV. CONCLUSION

This paper has proposed an accurate Doppler velocity–associated radar imaging scheme for the 79-GHz band MMW MIMO radar in a short-distance sensing application. Focusing on higher Doppler velocity resolution in the 79-GHz band, the proposed method introduces Doppler velocity space decomposition to realize accurate Doppler associated radar images. In addition, to overcome the limitation of the maximum velocity range due to STFT-based Doppler

velocity analysis, the WKD-based estimator is associated with the radar image, where the Doppler decomposition data are processed simultaneously in the WKD scheme to suppress inaccuracies caused by interference among multiple objects. The performance of the proposed method was assessed in two experimental validations involving three rotating metallic spheres and a real walking human. The results demonstrated that the proposed method achieved a more accurate Doppler velocity–associated radar image than those acquired by the existing method [21], [22]. Notably, the Doppler associated images would be useful in the post-human object recognition, such as based on the machine learning scheme [26]. Because the experimental validation assumed a short-distance sensing task (approximately 1 m), it would be more challenging to consider long-range sensing, e.g., greater than 10 m, to represent practical scenarios, such as automotive radar for collision avoidance. However, the proposed scheme has the potential to overcome the limited spatial resolution in traditional radar imaging by decomposing Doppler velocity components, which are also obtained by an accurate estimator, e.g., the WKD method. Thus, we are currently investigating the proposed method's efficacy for practical applications at longer ranges.

REFERENCES

[1] D. A. Andrews, S. W. Harmer, N. J. Bowring, N. D. Rezgui, and M. J. Southgate, "Active Millimeter Wave Sensor for Standoff Concealed Threat Detection", *IEEE Sensors Journal*, VOL. 13, NO. 12, pp. 4948–4955, DEC. 2013.

[2] Y. Kim, I. Alnujaim and D. Oh, "Human Activity Classification Based on Point Clouds Measured by Millimeter Wave MIMO Radar With Deep Recurrent Neural Networks," *IEEE Sensors Journal*, vol. 21, no. 12, pp. 13522-13529, 15 June15, 2021

[3] F. Soldovieri, A. Brancaccio, G. Prisco, G. Leone, and R. Pieri, "A Kirchhoff-based shape reconstruction algorithm for the multimonostatic configuration: The realistic case of buried pipes", *IEEE Trans. Geosci. and Remote Sens.*, vol. 46, no. 10, pp. 3031–3038, Oct., 2008.

[4] H. Sun, C. Gao, Z. Zhang, X. Liao, X. Wang and J. Yang, "High-Resolution Anisotropic Prestack Kirchhoff Dynamic Focused Beam Migration," in IEEE Sensors Journal, vol. 20, no. 20, pp. 11753-11760, 15 Oct.15, 2020

[5] J. M. Lopez-Sanchez and J. Fortuny-Guasch, "3-D radar imaging using range migration techniques," *IEEE Trans. Antennas & Propagat.*, vol. 48, no. 5, pp. 728-737, May 2000.

[6] Z. Wang, Q. Guo, X. Tian, T. Chang , and H. L. Cui, "Near-Field 3-D Millimeter-Wave Imaging Using MIMO RMA With Range Compensation", *IEEE Tran. Microwave Theory & Techniques*, VOL. 67, NO. 3, pp. 1157–1166, Mar., 2019.

This article has been accepted for publication in IEEE Sensors Journal. This is the author's version which has not been fully edited and
content may change prior to final publication. Citation information: DOI 10.1109/JSEN.2025.3547312

Y. SEKIGAWA *et al.*: DOPPLER ASSOCIATED 79 GHZ BAND MMW RADAR IMAGING   11

[7] X. Zhuge and A. G. Yarovoy, "Three-Dimensional Near-Field MIMO Array Imaging Using Range Migration Techniques," *IEEE Trans. Image Processing*, vol. 21, no. 6, pp. 3026-3033, June 2012.

[8] R. Zhu, J. Zhou, G. Jiang and Q. Fu, "Range Migration Algorithm for Near-Field MIMO-SAR Imaging," *IEEE Geosci. & Remote Sens. Lett.*, vol. 14, no. 12, pp. 2280-2284, Dec. 2017.

[9] L. Ding, S. Wu, P. Li and Y. Zhu, "Millimeter-Wave Sparse Imaging for Concealed Objects Based on Sparse Range Migration Algorithm," *IEEE Sensors Journal*, vol. 19, no. 16, pp. 6721-6728, 15 Aug.15, 2019

[10] J. Yang, *et al.*, "Compressed Sensing Radar Imaging With Magnitude Sparse Representation," *IEEE Access*, vol. 7, pp. 29722-29733, 2019.

[11] M. Miller, J. Hinze, M. Saquib and A. J. Blanchard, "Adjustable Transmitter Spacing for MIMO Radar Imaging With Compressed Sensing," in IEEE Sensors Journal, vol. 15, no. 11, pp. 6671-6677, Nov. 2015

[12] F. Gu, Q. Zhang, L. Chi, Y. Chen and S. Li, "A Novel Motion Compensating Method for MIMO-SAR Imaging Based on Compressed Sensing," in IEEE Sensors Journal, vol. 15, no. 4, pp. 2157-2165, April 2015

[13] S. Xu and A. Yarovoy, "Motion-Based Separation and Imaging of Closely Spaced Extended Targets," in IEEE Sensors Journal, vol. 20, no. 22, pp. 13542-13551, 15 Nov.15, 2020

[14] T. Wagner, R. Feger and A. Stelzer, "Radar Signal Processing for Jointly Estimating Tracks and Micro-Doppler Signatures," *IEEE Access*, vol. 5, pp. 1220-1238, 2017.

[15] Y. Ding, C. Lei, X. Xu, K. Sun and L. Wang, "Human Micro-Doppler Frequency Estimation Approach for Doppler Radar," *IEEE Access*, vol. 6, pp. 6149-6159, 2018.

[16] M. Li, T. Chen and H. Du, "Human Behavior Recognition Using Range-Velocity-Time Points," *IEEE Access*, vol. 8, pp. 37914-37925, 2020

[17] Y. Li, Z. Peng, R. Pal and C. Li, "Potential Active Shooter Detection Based on Radar Micro-Doppler and Range-Doppler Analysis Using Artificial Neural Network," in IEEE Sensors Journal, vol. 19, no. 3, pp. 1052-1063, 1 Feb.1, 2019

[18] S. Skaria, A. Al-Hourani, M. Lech and R. J. Evans, "Hand-Gesture Recognition Using Two-Antenna Doppler Radar With Deep Convolutional Neural Networks," in IEEE Sensors Journal, vol. 19, no. 8, pp. 3041-3048, 15 April15, 2019

[19] L. Du, Y. Ma, B. Wang and H. Liu, "Noise-Robust Classification of Ground Moving Targets Based on Time-Frequency Feature From Micro-Doppler Signature," in IEEE Sensors Journal, vol. 14, no. 8, pp. 2672-2682, Aug. 2014

[20] Z. Xu, C. J. Baker and S. Pooni, " Range and Doppler Cell Migration in Wideband Automotive Radar," *IEEE Trans. Vehicular Technology*, vol. 68, no. 6, pp. 5527-5536, June 2019.

[21] Y. Sekigawa and S. Kidera, "Doppler Velocity Decomposed Radar Imaging Method for 79 GHz Band Millimeter Wave Radar," *2022 International Symposium on Antennas and Propagation (ISAP)*, Sydney, Australia, 2022, pp. 3-4.

[22] Y. Sekigawa and S. Kidera, "Doppler velocity decomposition based radar imaging by 79 GHz band millimeter wave radar," *IEICE Transactions on Communications*, 2024.

[23] M. Setsu, T. Hayashi, J. He and S. Kidera, "Super-Resolution Doppler Velocity Estimation by Kernel-Based Range–τ Point Conversions for UWB Short-Range Radars," *IEEE Transactions on Geoscience and Remote Sensing*, vol. 58, no. 4, pp. 2430-2443, April 2020.

[24] T. Ando and S. Kidera, "k- and Doppler Velocity Decomposition-Based Range Points' Migration for 3-D Localization With Millimeter Wave Radar," *IEEE Sensors J.*, vol. 22, no. 23, pp. 22850-22864, Dec., 2022.

[25] S. Kidera, T. Sakamoto and T. Sato, "Accurate UWB Radar 3-D Imaging Algorithm for Complex Boundary without Wavefront Connection," *IEEE Trans. Geosci. and Remote Sens.*, vol. 48, no. 4, pp. 1993–2004, Apr., 2010.

[26] J. He, S. Terashima, H. Yamada and S. Kidera, "Diffraction Signal-Based Human Recognition in Non-Line-of-Sight (NLOS) Situation for Millimeter Wave Radar," *IEEE Journal of Selected Topics in Applied Earth Observations and Remote Sensing*, vol. 14, pp. 4370-4380, 2021.

Yoshiki Sekigawa received the B.E. degree in communication engineering and informatics from the University of Electro-Communications, Tokyo, Japan, in 2022, and received the M. E degree with the Graduate School of Informatics and Engineering, the University of Electro-Communications, Tokyo, Japan, in 2024. His research interest includes signal processing and imaging for millimeter wave radar as well as its applications. He joined the Mitsubishi Electric Corp., Japan, 2024.

Shouhei Kidera received his B.E. degree in Electrical and Electronic Engineering from Kyoto University in 2003 and M.I. and Ph.D. degrees in Informatics from Kyoto University, Kyoto, Japan, in 2005 and 2007, respectively. In 2009, he joined as an Assistant Professor with the University of Electro-Communications, Tokyo, Japan, where he is currently a full Professor with Graduate School of Informatics and Engineering in the University of Electro-Communications, Tokyo, Japan. His current research interest is in advanced radar signal processing or electromagnetic inverse scattering issue for ultra wideband (UWB) three-dimensional sensor or bio-medical applications. He has been stayed at the Cross-Disciplinary Electromagnetics Laboratory in the University of Wisconsin Madison as the visiting researcher in 2016. He has been a Principal Investigator of the PRESTO Program of Japan Science and Technology Agency (JST) from 2017 to 2021. He was a recipient of the 2012 Ando Incentive Prize for the Study of Electronics, 2013 Young Scientist's Prize by the Japanese Minister of Education, Culture, Sports, Science and Technology (MEXT), and 2014 Funai Achievement Award, 2022 KDDI Foundation Award, Contribution Award, and 2023 RIEC Award. He is a senior member of the Institute of Electronics, Information, and Communication Engineers of Japan (IEICE), and a member of the Institute of Electrical Engineering of Japan (IEEJ), and the Japan Society of Applied Physics (JSAP).